Solid solutions between lead fluorapatite and lead fluorvanadate apatite: compressibility determined by using a diamond-anvil cell coupled with synchrotron X-ray diffraction

Qiang He, Xi Liu, Xiaomin Hu, Liwei Deng, Zhiqiang Chen, Baosheng Li & Yingwei Fei

Physics and Chemistry of Minerals

ISSN 0342-1791
Volume 39
Number 3

Phys Chem Minerals (2012) 39:219-226
DOI 10.1007/s00269-011-0477-5

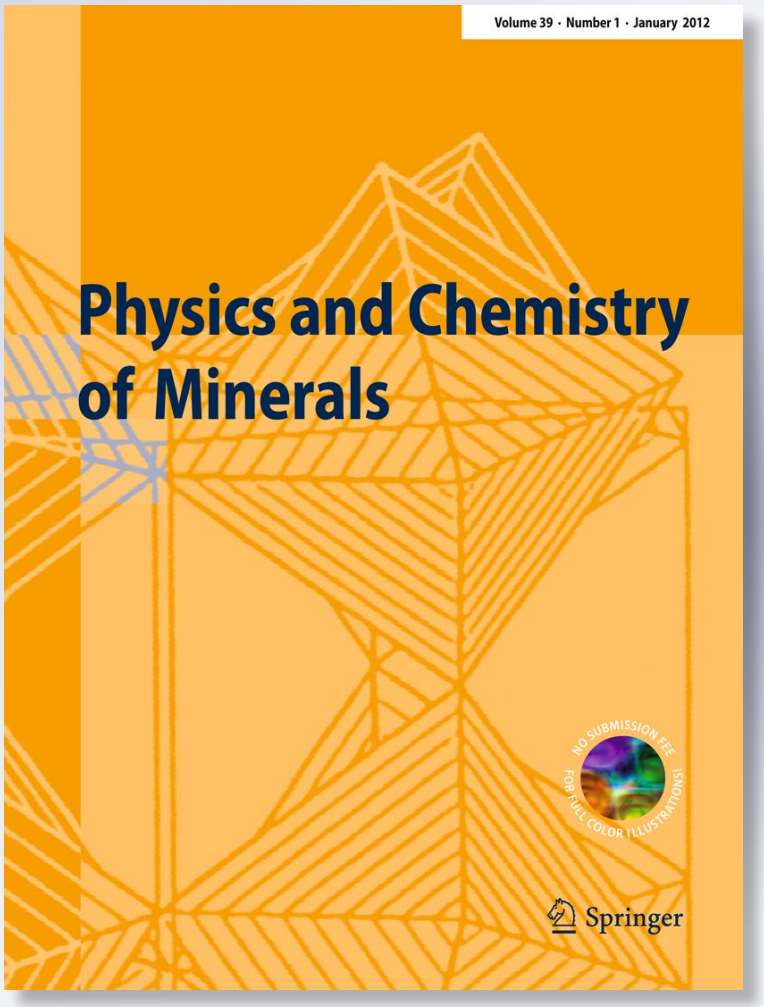

Springer

Phys Chem Minerals (2012) 39:219–226
DOI 10.1007/s00269-011-0477-5

ORIGINAL PAPER

Solid solutions between lead fluorapatite and lead fluorvanadate apatite: compressibility determined by using a diamond-anvil cell coupled with synchrotron X-ray diffraction

Qiang He · Xi Liu · Xiaomin Hu · Liwei Deng · Zhiqiang Chen · Baosheng Li · Yingwei Fei

Received: 31 October 2011 / Accepted: 17 December 2011 / Published online: 30 December 2011

Abstract The synthetic solid solutions between lead fluorapatite and lead fluorvanadate apatite, $Pb_{10}[(PO_4)_{6-x}(VO_4)_x]F_2$ with x equal to 0, 1, 2, 3, 4, 5, and 6, were compressed up to about 9 GPa at ambient temperature by using a diamond-anvil cell coupled with synchrotron X-ray radiation. A second-order Birch–Murnaghan equation of state was used to fit the data. As the substitution of the PO_4^{3-} cations by the VO_4^{3-} cations progresses, the isothermal bulk modulus steadily decreases, with a maximum reduction of about 16% (from 68.4(16) GPa for $Pb_{10}(PO_4)_6F_2$ to 57.2(28) GPa for $Pb_{10}(VO_4)_6F_2$). For the entire composition range, the a-axis dimension remains more compressible than the c-axis dimension, with the ratio of the axial bulk moduli (K_{T-c}:K_{T-a}) larger than 1. The ratio of K_{T-c} to K_{T-a} increases from about 1.04(4) to 1.23(14) as the composition parameter x increases from 0 to 6, suggesting that the apatite solid solutions $Pb_{10}[(PO_4)_{6-x}(VO_4)_x]F_2$ become more elastically anisotropic.

Keywords Apatite solid solutions · Diamond-anvil cell · Elastic anisotropy · Isothermal bulk modulus · Synchrotron X-ray diffraction

Q. He · X. Liu (✉) · X. Hu
Key Laboratory of Orogenic Belts and Crustal Evolution, MOE, Peking University, Beijing 100871, People's Republic of China
e-mail: xi.liu@pku.edu.cn

Q. He · X. Liu · X. Hu
School of Earth and Space Sciences, Peking University, Beijing 100871, People's Republic of China

L. Deng · Y. Fei
Geophysical Laboratory, Carnegie Institution of Washington, 5251 Broad Branch Road, NW, Washington, DC 20015, USA

Z. Chen
National Synchrotron Light Source, Brookhaven National Laboratory, Upton, New York 11973, USA

B. Li
Mineral Physics Institute, State University of New York, Stony Brook, New York 11794, USA

Introduction

The apatite group minerals, with a general chemical formula of $M1_4M2_6(BO_4)_6X_2$, have a hexagonal crystal structure in most cases (space group $P6_3/m$; Hughes and Rakovan 2002). In this structure, the isolated BO_4 tetrahedra ($z = 1/4, 3/4$) are linked by the M1 cations in ninefold (6 + 3) coordination and M2 cations in an irregular sevenfold (6 + 1) coordination. The triclusters of M2 cations form large c-axis channels, where the X anions locate. Previous investigations show that extensive chemical substitutions take place at all these different crystallographic sites (Pan and Fleet 2002, and references therein), with the M1 and M2 sites primarily occupied by large cations such as Na^+, Ca^{2+}, Mn^{2+}, Cd^{2+}, Ba^{2+}, Sr^{2+}, Pb^{2+}, Al^{3+} and rare-earth elements (REE^{3+}), the B-site commonly by P^{5+}, V^{5+}, As^{5+}, S^{6+}, and Si^{4+}, and the X-site by halides, hydrogen-carbonate cation (Fleet and Liu 2007), oxy-anions, vacancies and small neutral molecules such as H_2O. It is thus very interesting to probe the relationship between the crystal chemistry and the physical–chemical properties of the apatites.

It has been experimentally demonstrated that hydroxylapatite and fluorapatite are stable up to about 12 GPa (Murayama et al. 1986). Since substantial amounts of trace elements can be hosted by the apatite structure (Fleet and Pan 1997; Fleet et al. 2000a, b; Klemme and Dalpé 2003;

Prowatke and Klemme 2006), apatites have the capability to bring down into the Earth's upper mantle large quantities of trace elements, which should lead to some important geochemical heterogeneity in the mantle. For a mineral, its capability of hosting certain trace elements is closely related to its elastic behavior, as suggested by the lattice strain model (Blundy and Wood 1994). Indeed, investigations of different types have been conducted to explore the elasticity of apatites with different compositions (Yoon and Newnham 1969; Gilmore and Katz 1982; Sha et al. 1994; Teraoka et al. 1998; Brunet et al. 1999; Comodi et al. 2001a, b; Matsukage et al. 2004; Snyders et al. 2007; Liu et al. 2008, 2011a, b; Ching et al. 2009; Gatta et al. 2009; Fleet et al. 2010; He et al. 2011). The existing studies, however, have mostly focused on the effect of the cation substitutions on the M-sites and X-sites of the apatite structure on the apatite elasticity. The influence of the B-site substitution remains undisclosed.

Recently, a series of lead apatite solid solutions of the composition $Pb_{10}[(PO_4)_{6-x}(VO_4)_x]F_2$ ($x = 0$, 1, 2, 3, 4, 5 and 6) was synthesized by solid-state reaction at 1 atm and 700°C (He et al. 2011). With a continuous B-site substitution between the PO_4^{3-} cations and the VO_4^{3-} cations, this series of apatites has given us a good opportunity to investigate the relationship between the B-site composition variation and the elastic features of the apatites.

Experiment

The apatite solid solution series, with the composition of $Pb_{10}[(PO_4)_{6-x}(VO_4)_x]F_2$ (x designed as 0, 1, 2, 3, 4, 5 and 6), was synthesized in a conventional muffle furnace via solid-state reaction at 1 atm and 700°C for 72 h (He et al. 2011). The textures of the synthetic products were characterized by using optical microscopy and scanning electron microscopy (SEM; Quanta 200 FEG). Their crystal structure was confirmed by using powder X-ray diffraction method (XRD; X'Pert Pro MPD system) and Raman spectroscopy. Their compositions were confirmed by using electron microprobe analysis (EMPA; JEOL JXA-8100). The mixing behavior between the PO_4^{3-} cations and the VO_4^{3-} cations on the B-sites of the apatites was detailed by using powder X-ray diffraction and Raman spectroscopy. In addition, the thermal elasticity of these apatites was investigated up to 600°C at ambient pressure (He et al. 2011).

In this investigation, we conducted in situ high-pressure angle dispersive X-ray diffraction experiments at the beamline X17C, National Synchrotron Light Source, Brookhaven National Laboratory. We generated the high pressure by using a symmetrical diamond-anvil cell. In these high-P experiments, T301 stainless steel plates with an initial thickness of 250 μm were used as gaskets, with their central part pre-indented to a thickness of about 40 μm and then drilled through into a hole of 150 μm in diameter. The finely ground apatite powder, plus a couple of tiny ruby balls, was loaded with the liquid pressure medium (a 4:1 methanol-ethanol mixture) into the hole in the gasket. The ruby fluorescence method (Mao et al. 1978) was employed to determine the experimental pressure. The wavelength of the incident synchrotron radiation beam was 0.4066 Å and the beam size was $\sim 25 \times 20$ μm^2. An online CCD detector was used to collect the X-ray diffraction patterns (collecting time = 10 min), which were later integrated to generate the conventional one-dimensional profiles using the Fit2D program (Hammersley 1996). With a full profile refinement of the collected powder X-ray data, the positions of the diffraction peaks 110, 200, 111, 002, 102, 210, 211, 112, 300, 221, 302, 113, 400, 222, 312, 320, 213, 321, 410, 303, 004, 420, 331, 214, 502, 323, 511 and 332 were determined and later used to derive the unit-cell parameters of the apatites at different pressures. These experimental and data-processing techniques were well established in our previous studies (Liu et al. 2008, 2009, 2011a, b; Fleet et al. 2010).

Results and discussion

Hydrostatic or quasi-hydrostatic high-P experiments at ambient temperature were conducted with the $Pb_{10}[(PO_4)_{6-x}(VO_4)_x]F_2$ apatite solid solutions ($x = 1$, 2, 3, 4, 5 and 6) up to about 8.57 GPa (Table 1). The pressure quality in most high-P experiments was hydrostatic, but in some cases at relatively high pressures, it was probably just quasi-hydrostatic, as presumably suggested by the peak-broadening phenomenon shown in Fig. 1a. Since the 4:1 methanol–ethanol mixture should remain as a liquid at pressures below about 10 GPa (Klotz et al. 2009), the potentially relatively poor pressure quality at relatively high pressures might suggest a leakage of the pressure medium. Lucky enough, lead apatites themselves are relatively soft materials (Liu et al. 2008, 2011a; Fleet et al. 2010), so that the pressure quality even in those worst cases was still bearable. Alternatively, however, the peak-broadening phenomenon observed at relatively high pressures might just indicate an approaching phase transition or phase decomposition, which was somehow hindered due to slow reaction rate at ambient temperature. Murayama et al. (1986) experimentally demonstrated that hydroxylapatite and fluorapatite are stable up to about 12 GPa only, and we speculate that the pressure stability of the $Pb_{10}[(PO_4)_{6-x}(VO_4)_x]F_2$ apatite solid solutions might be more or less reduced, probably close to the high values of the pressures in our experiments.

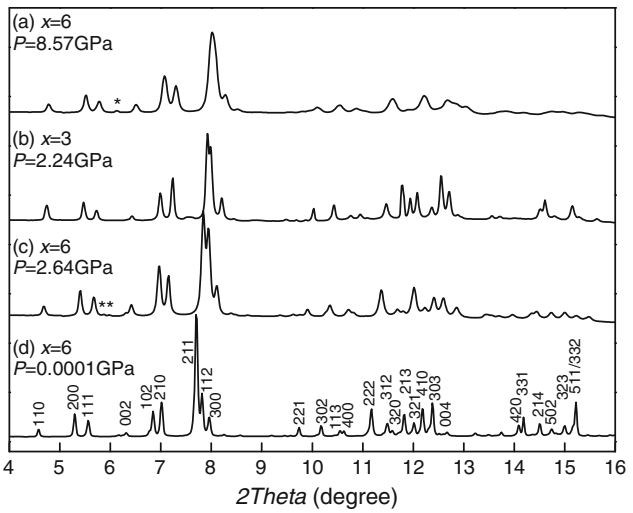

Fig. 1 Examples of synchrotron X-ray diffraction patterns for the $Pb_{10}[(PO_4)_{6-x}(VO_4)_x]F_2$ apatite solid solutions at different pressures: (*a*) $x = 6$ and $P = 8.57$ GPa; (*b*) $x = 3$ and $P = 2.24$ GPa; (*c*) $x = 6$ and $P = 2.64$ GPa; (*d*) $x = 6$ and $P = 0.0001$ GPa. Note the peak-broadening in (*a*), and the extra weak peaks (denoted by the asterisks in *a* and *c*) which do not belong to the apatite structure. One potential origin of these extra weak peaks is that the particle size of the $Pb_{10}(VO_4)_6F_2$-apatite powder might be slightly coarser than what is appropriate for the synchrotron X-ray radiation with short wavelength. It is well known that coarse particles produce erratic black spots on the X-ray diffraction patterns collected by the CCD detector, which, as integrated, bring forth some extra weak peaks on the one-dimensional X-ray profile. The other possibility is that they might be attributed to the minor amount of impurity phase in the sample (He et al. 2011)

In total, we collected 43 in situ powder X-ray diffraction patterns, some of which are shown as examples in Fig. 1. All the observed major X-ray diffraction peaks in these X-ray diffraction patterns can be attributed to the apatite structure, suggesting that the $Pb_{10}[(PO_4)_{6-x}(VO_4)_x]F_2$ apatite solid solutions are stable (or metastable due to potential kinetic reason) within the investigated pressure range. Previous compression experiments at ambient temperature conducted with apatites of different compositions up to much higher pressures also did not show any concrete evidence to any phase transition (Brunet et al. 1999; Liu et al. 2008, 2011a; Fleet et al. 2010). Additionally, data collected both during compression and during decompression did not show any significant difference, indicating the full reversibility of the elastic behavior of these apatites. The derived unit-cell parameters are listed in Table 1 and plotted in Fig. 2.

Apparently, high pressure reduces the dimensions of the unit cells of the $Pb_{10}[(PO_4)_{6-x}(VO_4)_x]F_2$ apatite solid solutions, as suggested by the negative slopes of the *P–V* correlation curves (Fig. 2). In detail, the average slopes of these *P–V* correlation curves become more negative as the VO_4^{3-} content increases, which means that the VO_4^{3-}-poor apatites are less compressible than the VO_4^{3-}-rich apatites (more discussion later). Since the effective ionic radius of V^{5+} for fourfold coordination (0.355 Å) is much larger than that of P^{5+} (0.17 Å; Shannon 1976), the VO_4^{3-} tetrahedron should be significantly larger than the PO_4^{3-} tetrahedron (Mercier et al. 2007). Indeed, with the progressing substitution of P^{5+} by V^{5+}, the Raman vibration frequencies of both the VO_4^{3-} and PO_4^{3-} cations linearly decrease (He et al. 2011), which suggests a smooth increase in the bond distances of the V–O and P–O chemical bonds, respectively (Hardcastle and Wachs 1991; Popović et al. 2005). As well known, longer bond distance indicates weaker bond in general, so that both the VO_4^{3-} and PO_4^{3-} tetrahedra become more compressible, which in turn leads to the increasing bulk compressibility as shown in Fig. 2.

For the apatites poor in VO_4^{3-}, the compressibility of their *a*-axis is much comparable to that of the *c*-axis, as illustrated by the general overlapping of their correlation curves (P-a/a_0 and P–c/c_0) in Fig. 2a, 2b and 2c. This observation is in excellent agreement with Liu et al. (2008) and Fleet et al. (2010), in which a nearly isotropic elasticity was observed for the lead fluorapatite $Pb_{10}(PO_4)_6F_2$. As the VO_4^{3-} content increases, the *a*-axis becomes more compressible than the *c*-axis, as shown by the larger average negative slopes of the P-a/a_0 curves than those of the P–c/c_0 curves in Fig. 2d, 2e and 2f. This effect of composition on the elasticity of the $Pb_{10}[(PO_4)_{6-x}(VO_4)_x]F_2$ apatite solid solutions is also verified by the slopes of the correlation curves between the ratio of $(c/a)/(c_0/a_0)$ and pressure, which are very close to 1 at low VO_4^{3-} contents (Fig. 2a, 2b and 2c), but significantly larger than 1 at high VO_4^{3-} contents (Fig. 2d, 2e and 2f). This should be anticipated since the replacement of P^{5+} by V^{5+} cations always significantly increases the *a*-axis dimension but leaves the *c*-axis dimension increased little ($Ca_{10}[(PO_4)_{6-x}(VO_4)_x](OH)_2$ solid solutions, Boechat et al. 2000; $Pb_{10}[(PO_4)_{6-x}(VO_4)_x]Cl_2$ solid solutions, Chernorukov et al. 2010; $Pb_{10}[(PO_4)_{6-x}(VO_4)_x]F_2$ solid solutions, He et al. 2011).

The *P–V* data of the $Pb_{10}[(PO_4)_{6-x}(VO_4)_x]F_2$ apatite solid solutions have been fitted to the second-order Birch–Murnaghan equation of state by a least-squares method to derive the isothermal bulk modulus (Birch 1947):

$$P = 3K_T f_E (1 + 2f_E)^{\frac{5}{2}}$$

where P is the pressure, K_T the isothermal bulk modulus, and f_E the Eulerian definition of finite strain, which is $[(V_0/V)^{2/3}-1]/2$, respectively. In the Eulerian definition of finite strain, V_0 is the volume at zero pressure, whereas V is the volume at high pressure. In addition, a second-order Birch–Murnaghan-type equation of state proposed by

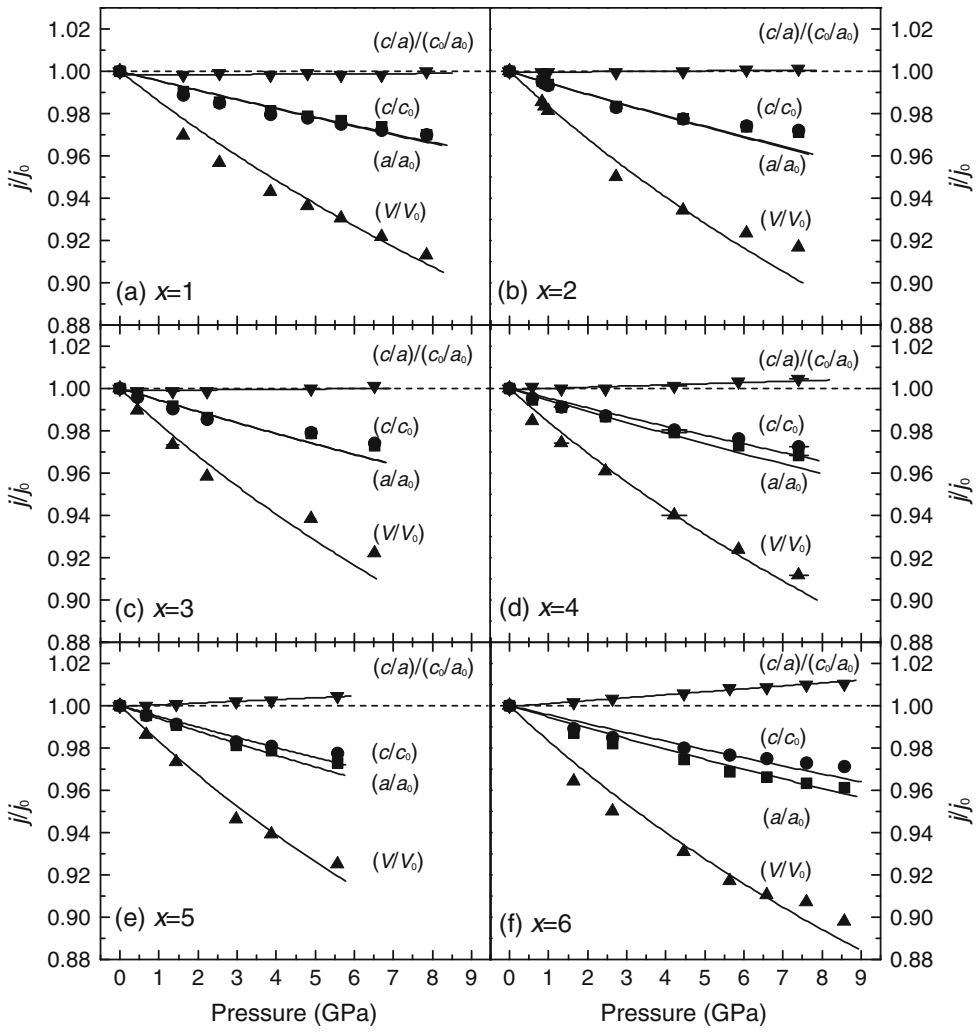

Fig. 2 Variations in lattice parameters with change in pressure: (*a*) $x = 1$; (*b*) $x = 2$; (*c*) $x = 3$; (*d*) $x = 4$; (*e*) $x = 5$; (*f*) $x = 6$. *j* stands for *a*, *c*, *V* or *c*/*a* at high pressure, whereas j_0 stands for a_0, c_0, V_0 or c_0/a_0 at room pressure. The curves of a/a_0-*P*, c/c_0-*P* and V/V_0-*P* represent the second-order Birch–Murnaghan equations of state for the $Pb_{10}[(PO_4)_{6-x}(VO_4)_x]F_2$ apatite solid solutions (see Table 2 for the parameters). The lines of $(c/a)/(c_0/a_0)$-*P* were derived by a weighted linear regression

Angel (2000) was used to obtain the parameters of the equations of state along the *a*- and *c*-axes, called as K_{T-a} and K_{T-c}, respectively. The derived parameters are summarized in Table 2.

It should be noted that a third-order Birch–Murnaghan equation of state with variable K_T' (the first pressure derivative of the isothermal bulk modulus) might be slightly better to fit our *P*–*V* data, as implied by the experimental investigations of Liu et al. (2008), Gatta et al. (2009) and Liu et al. (2011a). Taking into consideration the narrow pressure ranges of our experiments, the quality of our *P*–*V* data, and our purpose to demonstrate the composition influence on the elastic behavior of the $Pb_{10}[(PO_4)_{6-x}(VO_4)_x]F_2$ apatite solid solutions, we believe that the second-order Birch–Murnaghan equation of state is good enough to describe the experimental data.

As shown in Fig. 3a, the replacement of PO_4^{3-} by VO_4^{3-} on the B-sites in the $Pb_{10}[(PO_4)_{6-x}(VO_4)_x]F_2$ apatite solid solutions causes the isothermal bulk modulus to decrease. For a full replacement, the maximum decrease in the isothermal bulk modulus is about 16% (from 68.4(16) GPa for $Pb_{10}(PO_4)_6F_2$ to 57.2(28) GPa for $Pb_{10}(VO_4)_6F_2$; Table 2). Previous investigation done by Liu et al. (2008) demonstrated that a full replacement of Ca by Pb on the M-sites of the fluorapatite causes a 25% reduction of the isothermal bulk modulus (91.5(38) GPa for $Ca_{10}(PO_4)_6F_2$ and 68.4(16) GPa for $Pb_{10}(PO_4)_6F_2$; Matsukage et al. 2004; Liu et al. 2008). For the substitution of F, Cl, and OH on the X-sites, however, Brunet et al. (1999) demonstrated that the variation of the bulk moduli is very limited, commonly less than 5% ($Ca_{10}(PO_4)_6[F,Cl,OH]_2$). The small effect of the composition variation of the X-sites on the bulk modulus probably also holds for the lead apatites, as suggested by the small difference between the bulk moduli of $Pb_{10}(VO_4)_6F_2$ (57.2(28) GPa; this study) and $Pb_{10}(VO_4)_6Cl_2$ (58.6(12) GPa; Gatta et al. 2009). Presumably, due to the much larger size of Br compared to that of F, Cl, or OH, on the other hand, the bulk modulus of $Pb_{10}(PO_4)_6Br_2$ is about 60.8(11) GPa (Liu et al. 2011a), about 11% smaller than that of $Pb_{10}(PO_4)_6F_2$ (Table 2).

Table 1 Unit-cell parameters of the apatite solid solutions $Pb_{10}[(PO_4)_{6-x}(VO_4)_x]F_2$ at high pressures and room temperature

P (GPa)[a]	a (Å)	c (Å)	V (Å^3)	c/a
$x = 1$				
0.0001[b]	9.831 (2)[c]	7.328 (2)	613.3 (2)	0.7454 (3)
1.62 (5)	9.736 (1)	7.245 (1)	594.7 (1)	0.7442 (2)
2.56 (5)	9.690 (3)	7.218 (3)	586.9 (3)	0.7449 (4)
3.86 (4)	9.645 (1)	7.177 (0)	578.2 (1)	0.7441 (1)
4.80 (0)	9.621 (1)	7.165 (1)	574.3 (1)	0.7447 (1)
5.67 (3)	9.603 (1)	7.146 (2)	570.7 (2)	0.7441 (2)
6.69 (5)	9.573 (1)	7.123 (1)	565.3 (1)	0.7441 (2)
7.85 (5)	9.537 (1)	7.109 (1)	560.0 (1)	0.7454 (2)
$x = 2$				
0.0001[b]	9.888 (2)	7.329 (1)	620.5 (1)	0.7412 (2)
0.84 (5)	9.841 (2)	7.291 (1)	611.5 (1)	0.7408 (2)
0.89 (0)	9.836 (3)	7.285 (1)	610.3 (2)	0.7406 (2)
1.00 (6)[d]	9.826 (3)	7.281 (1)	608.9 (2)	0.7410 (2)
2.73 (3)	9.722 (2)	7.202 (1)	589.5 (1)	0.7408 (1)
4.44 (6)[d]	9.666 (3)	7.163 (1)	579.7 (2)	0.7411 (2)
6.07 (11)	9.627 (3)	7.140 (1)	573.0 (2)	0.7417 (3)
7.40 (8)	9.602 (3)	7.125 (1)	568.9 (2)	0.7420 (3)
$x = 3$				
0.0001[b]	9.975 (1)	7.354 (2)	633.7 (2)	0.7373 (2)
0.45 (3)[d]	9.944 (1)	7.323 (1)	627.1 (1)	0.7364 (1)
1.35 (15)	9.890 (1)	7.283 (1)	616.9 (0)	0.7364 (1)
2.24 (0)	9.838 (1)	7.246 (2)	607.4 (2)	0.7365 (2)
4.91 (11)	9.765 (2)	7.200 (2)	594.5 (3)	0.7374 (3)
6.53 (0)	9.704 (3)	7.164 (4)	584.2 (4)	0.7382 (5)
$x = 4$				
0.0001[b]	10.024 (2)	7.356 (3)	640.2 (2)	0.7339 (3)
0.58 (5)[d]	9.971 (1)	7.322 (1)	630.4 (1)	0.7344 (1)
1.33 (18)	9.937 (1)	7.293 (1)	623.7 (1)	0.7339 (1)
2.45 (5)	9.891 (1)	7.260 (1)	615.1 (1)	0.7340 (1)
4.22 (32)	9.816 (1)	7.212 (1)	601.8 (1)	0.7347 (1)
5.86 (11)	9.751 (1)	7.181 (1)	591.3 (2)	0.7364 (2)
7.41 (23)	9.706 (2)	7.154 (2)	583.6 (3)	0.7371 (3)
$x = 5$				
0.0001[b]	10.097 (2)	7.374 (2)	651.0 (3)	0.7303 (3)
0.69 (6)	10.050 (1)	7.341 (1)	642.1 (1)	0.7304 (1)
1.44 (3)	10.004 (1)	7.311 (1)	633.7 (1)	0.7308 (1)
2.97 (0)	9.906 (1)	7.248 (1)	615.9 (2)	0.7317 (1)
3.89 (3)	9.881 (2)	7.233 (1)	611.5 (2)	0.7320 (2)
5.57 (2)	9.822 (1)	7.207 (2)	602.1 (2)	0.7338 (2)
$x = 6$				
0.0001[b]	10.137 (8)	7.372 (1)	656.0 (1)	0.7272 (6)
1.65 (2)	10.008 (1)	7.291 (1)	632.4 (1)	0.7285 (1)
2.64 (3)	9.954 (1)	7.262 (1)	623.1 (1)	0.7295 (1)
4.46 (3)	9.878 (1)	7.225 (1)	610.5 (1)	0.7314 (1)
5.64 (0)[d]	9.821 (1)	7.200 (1)	601.5 (2)	0.7331 (2)
6.59 (0)[d]	9.795 (1)	7.186 (2)	597.1 (2)	0.7337 (2)
7.61 (8)[d]	9.763 (2)	7.172 (2)	595.1 (3)	0.7346 (3)

Table 1 continued

P (GPa)[a]	a (Å)	c (Å)	V (Å^3)	c/a
8.57 (3)	9.746 (2)	7.161 (3)	589.1 (3)	0.7348 (3)

[a] Pressure determined by averaging the values measured before and after collection of synchrotron data

[b] Data at ambient pressure collected on powder sample loosely packed into a small hole (400 μm across) in a stainless steel plate

[c] Numbers in parentheses representing one standard deviation

[d] Data collected during decompression

Table 2 Volumetric and axial bulk moduli of some lead apatites at room pressure and room temperature

Composition	K_T (GPa)	K_{T-a} (GPa)	K_{T-c} (GPa)	Data source
$Pb_{10}(PO_4)_6F_2$	68.4 (16)[a]	68.1 (11)[b]	71.8 (30)	Liu et al. (2008)
$Pb_{10}[(PO_4)_5(VO_4)_1]F_2$	67.9 (38)	71.8 (45)	72.9 (70)	This study
$Pb_{10}[(PO_4)_4(VO_4)_2]F_2$	57.7 (45)	59.2 (47)	60.1 (61)	This study
$Pb_{10}[(PO_4)_3(VO_4)_3]F_2$	57.7 (62)	59.1 (57)	59.4 (82)	This study
$Pb_{10}[(PO_4)_2(VO_4)_4]F_2$	60.6 (32)	59.8 (29)	71.3 (49)	This study
$Pb_{10}[(PO_4)_1(VO_4)_5]F_2$	56.0 (58)	53.5 (47)	64.0 (82)	This study
$Pb_{10}(VO_4)_6F_2$	57.2 (28)	61.7 (31)	76.1 (75)	This study
$Pb_{10}(PO_4)_6Br_2$	60.8 (11)	56.6 (8)	77.9 (50)	Liu et al. (2011a)
$Pb_{10}(VO_4)_6Cl_2$	58.6 (12)	46.5 (10)	110.7 (14)	Gatta et al. (2009)

Second-order Birch–Murnaghan equation of state employed in the data-fitting, which used the unit-cell parameters at pressures below 10 GPa only

[a] Numbers in parentheses representing one standard deviation

[b] K_{T-a} of $Pb_{10}(PO_4)_6F_2$ obtained here by reprocessing the data from Liu et al. (2008) is very different to that obtained in Liu et al. (2011a; 92.7(148) GPa). An error occurred when Liu et al. (2011a) reprocessed the data from Liu et al. (2008): the a-axis at 9.42 GPa was mistakenly input as 9.497 Å, rather than the correct value of 9.397 Å

Similarly, the bulk modulus of the carbonated apatite LM005 is much smaller than that of carbonate-free hydroxylapatite ($\sim$ 20%; Liu et al. 2011b), due to the large size of the carbonate cation.

Figure 3b suggests that the replacement of PO_4^{3-} by VO_4^{3-} on the B-sites in the $Pb_{10}[(PO_4)_{6-x}(VO_4)_x]F_2$ apatite solid solutions also reduces the a-axial isothermal bulk modulus, with a maximum of about 15% for a full replacement. For the c-axial isothermal bulk modulus, however, the reduction with a full replacement is much smaller, maximally about 2.6% only (Fig. 3c). The ratio of the K_{T-c} and K_{T-a} thus increases from 1.04(4) to about 1.23(14), and its composition dependence can be empirically described by the equation $K_{T-c}{:}K_{T-a} = 1.04(4) + 0.03(2)x$ (Fig. 3d). As mentioned before, this increasing elastic anisotropy is mostly related to the different influences of the PO_4^{3-} and VO_4^{3-} cations on the crystal structure of the $Pb_{10}[(PO_4)_{6-x}(VO_4)_x]F_2$ apatite solid solutions: the full replacement of P by V causes the a-axis dimension to expand by about 3.4%, but leaves the c-axis dimension generally unchanged (He et al. 2011). Recently, He et al. (2011, Table 5) investigated the thermal expansivity of the $Pb_{10}[(PO_4)_{6-x}(VO_4)_x]F_2$ apatite solid solutions up to 600°C and found that the ratio of the thermal expansion coefficients along the c-axis and a-axis increases from about 1.23(5) to 1.49(6) as the replacement of the PO_4^{3-} cations by the VO_4^{3-} cations progresses, indicating an increasing elastic anisotropy as well.

The increasing elastic anisotropy of the $Pb_{10}[(PO_4)_{6-x}(VO_4)_x]F_2$ apatite solid solutions resulted in by the progressive substitution of PO_4^{3-} with VO_4^{3-} can be well explained by the role of the BO_4 cations in the apatite structure ($M1_4M2_6(BO_4)_6X_2$; space group $P6_3/m$ in general; Hughes and Rakovan 2002). Along the c-axis, the M1 atoms form chains and play a dominant role in deciding the c-axis dimension; the small, rigid, and isolated BO_4 cations attach to the $M1O_6$ metaprism via corner-connecting, so that their influence on the c-axis dimension is minor. In the (001) plane normal to the c-axis, in contrast, the BO_4 cations link together the $M1O_6$ and $M2O_6$ units and become structurally important. With these unmatched roles of the BO_4 cations in the directions along and normal to the c-axis, any compositional variation on the B-sites should lead to a change in the elasticity of the apatites. Since the $Pb_{10}(PO_4)_6F_2$-apatite is almost elastically isotropic (Liu et al. 2008; Fleet et al. 2010), a change in the elasticity

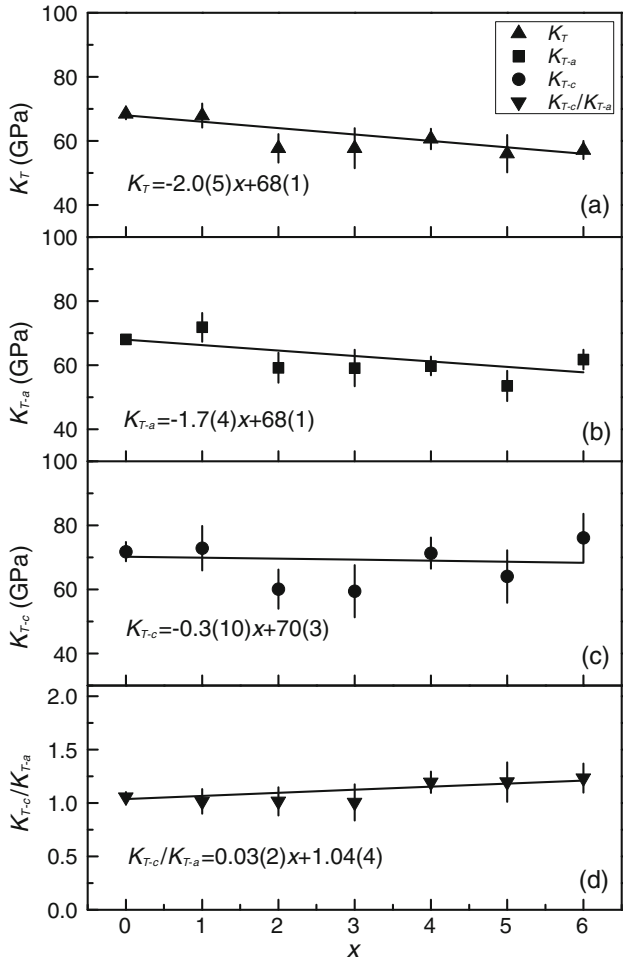

Fig. 3 Effect of composition on the compressibility of the $Pb_{10}[(PO_4)_{6-x}(VO_4)_x]F_2$ apatite solid solutions at ambient temperature and pressure: (*a*) K_T; (*b*) K_{T-a}; (*c*) K_{T-c}; (*d*) K_{T-c}/K_{T-a}

means an increasing of elastic anisotropy as the replacement of PO_4^{3-} by VO_4^{3-} advances. In this case, a larger compressibility or expansivity in the direction normal to the *c*-axis should be expected because the VO_4^{3-} cation is larger than the PO_4^{3-} cation.

The compositional difference on the X-sites can also affect the elastic behavior of the lead apatites. For the lead apatites $Pb_{10}(VO_4)_6F_2$ and $Pb_{10}(VO_4)_6Cl_2$, the K_{T-c}:K_{T-a} value of the former is about 1.23(14) whereas that of the latter is much larger, about 2.38(6) (Gatta et al. 2009). On the other hand, the lead apatite $Pb_{10}(PO_4)_6F_2$ has a K_{T-c}:K_{T-a} ratio of about 1.04(4), while the lead apatite $Pb_{10}(PO_4)_6Br_2$ has a ratio of 1.38(9) (Liu et al. 2011a). As discussed in Liu et al. (2011a), the replacement of F by Br causes the Pb2 cation and PO_4 tetrahedron to laterally shift away from the *c*-axis, which should significantly soften the *a*-axis dimension of the apatites. In the case of the *c*-axis, the 6s electrons of the Pb2 atoms might be directed toward the center of the *c*-axis channel, which in turn pushes the X cations out of the Pb2 triangles (Kim et al. 2000), and reduces the compressibility of the *c*-axis dimension as well. Without any detailed crystallographic study on the lead apatites of $Pb_{10}(VO_4)_6F_2$, $Pb_{10}(VO_4)_6Cl_2$, and $Pb_{10}(VO_4)_6Br_2$, it still appears reasonable to conclude that a large size of the cation on the X-sites of the lead apatites leads to a large elastic anisotropy.

Acknowledgments We are grateful to two anonymous reviewers and Professor M. Matsui who provided us with constructive comments which substantially improved the quality of our paper. We thank the National Natural Science Foundation of China (Grant 40872033 and 41090371) for financial support.

References

Angel RJ (2000) Equation of state. In: Hazen RM, Downs RT (eds) High-temperature and high-pressure crystal chemistry. Reviews in mineralogy and geochemistry, vol 41. Mineralogical Society of America, Chantilly, pp 35–60

Birch F (1947) Finite elastic strain of cubic crystals. Phys Rev 71:809–924

Blundy JD, Wood BJ (1994) Prediction of crystal-melt partition coefficients from elastic moduli. Nature 372:452–454

Boechat CB, Eon J-G, Rossi AM, Perez CAD, San Gil RAD (2000) Structure of vanadate in calcium phosphate and vanadate apatite solid solutions. Phys Chem Chem Phys 2:4225–4230

Brunet F, Allan DR, Redfern SAT, Angel RJ, Miletich RM, Reichmann HJ, Sergent J, Hanfland M (1999) Compressibility and thermal expansivity of synthetic apatites, $Ca_5(PO_4)_3X$ with X = OH, F and Cl. Eur J Miner 11:1023–1035

Chernorukov NG, Knyazev AV, Bulanov EN (2010) Isomorphism and phase diagram of the $Pb_5(PO_4)_3Cl$-$Pb_5(VO_4)_3Cl$ system. Russ J Inorg Chem 55:1463–1470

Ching WY, Rulis P, Misra A (2009) Ab initio elastic properties and tensile strength of crystalline hydroxyapatite. Acta Biomater 5:3067–3075

Comodi P, Liu Y, Zanazzi PF, Montagnoli M (2001a) Structural and vibrational behaviour of fluorapatite with pressure. Part I: in situ single-crystal X-ray diffraction investigation. Phys Chem Miner 28:219–224

Comodi P, Liu Y, Frezzotti ML (2001b) Structural and vibrational behaviour of fluorapatite with pressure. Part II: in situ micro-raman spectroscopic investigation. Phys Chem Miner 28:225–231

Fleet ME, Liu X (2007) Hydrogen-carbonate ion in synthetic high-pressure apatite. Am Miner 92:1764–1767

Fleet ME, Pan Y (1997) Rare earth elements in apatite: uptake from H_2O-bearing phosphate-fluoride melts and the role of volatile components. Geochim Cosmochim Acta 61:4745–4760

Fleet ME, Liu X, Pan Y (2000a) Site preference of rare earth elements in hydroxyapatite [$Ca_{10}(PO_4)_6(OH)_2$]. J Solid State Chem 149:391–398

Fleet ME, Liu X, Pan Y (2000b) Rare-earth elements in chlorapatite [$Ca_{10}(PO_4)_6Cl_2$]: uptake, site preference, and degradation of monoclinic structure. Am Miner 85:1437–1446

Fleet ME, Liu X, Shieh SR (2010) Structural change in lead fluorapatite at high pressure. Phys Chem Miner 37:1–9

Gatta GD, Lee Y, Kao CC (2009) Elastic behavior of vanadinite, $Pb_{10}(VO_4)_6Cl_2$, a microporous non-zeolitic mineral. Phys Chem Miner 36:311–317

Gilmore RS, Katz JL (1982) Elastic properties of apatites. J Mater Sci 17:1131–1141

Hammersley J (1996) Fit2D report. Europe Synchrotron Radiation Facility, Grenoble, France

Hardcastle FD, Wachs IE (1991) Determination of vanadium-oxygen bond distances and bond orders by Raman spectroscopy. J Phys Chem 95:5031–5041

He Q, Liu X, Hu X, Li S, Wang H (2011) Solid solution between lead fluorapatite and lead fluorvanadate apatite: mixing behavior, Raman feature and thermal expansivity. Phys Chem Miner 38:741–752

Hughes JM, Rakovan J (2002) The crystal structure of apatite, $Ca_5(PO4)_3$(F, OH, Cl). In: Kohn MJ, Rakovan J, Hughes JM (eds) Phosphates. Reviews in Mineralogy and Geochemistry, vol 48. Mineralogical Society of America, Chantilly, pp 1–12

Kim JY, Fenton RR, Hunter BA, Kennedy BJ (2000) Powder diffraction studies of synthetic calcium and lead apatites. Aust J Chem 53:679–686

Klemme S, Dalpé C (2003) Trace-element partitioning between apatite and carbonatite melt. Am Miner 88:639–646

Klotz S, Chervin JC, Munsch P, Le Marchand G (2009) Hydrostatic limits of 11 pressure transmitting media. J Phys D Appl Phys 42:075413

Liu X, Shieh SR, Fleet ME, Akhmetov A (2008) High-pressure study on lead fluorapatite. Am Miner 93:1581–1584

Liu X, Shieh SR, Fleet ME, Zhang L (2009) Compressibility of a natural kyanite at 300 K. Prog Nat Sci 19:1281–1286

Liu X, Fleet ME, Shieh SR, He Q (2011a) Synthetic lead bromapatite: X-ray structure at ambient pressure and compressibility up to about 20 GPa. Phys Chem Miner 38:397–406

Liu X, Shieh SR, Fleet ME, Zhang L, He Q (2011b) Equation of state of carbonated hydroxylapatite at ambient temperature: significance of carbonate. Am Miner 96:74–80

Mao HK, Bell PM, Shaner JW, Steinberg DJ (1978) Specific volume measurements of Cu, Mo, Pt, and Au and calibration of rub R1 fluorescence pressure gauge for 0.006–1 Mbar. J Appl Phys 49:3276–3283

Matsukage KN, Ono S, Kawamoto T, Kikegawa T (2004) The compressibility of a natural apatite. Phys Chem Miner 31:580–584

Mercier PHJ, Dong J, Baikie T, Page YL, White TJ, Whitfield PS, Mitchel LD (2007) Ab initio constrained crystal-chemical Rietveld refinement of $Ca_{10}(V_xP_{1-x}O_4)_6F_2$ apatites. Acta Cryst B63:37–48

Murayama JK, Nakai S, Kato M, Kumazawa M (1986) A dense polymorph of $Ca_3(PO_4)_2$: a high pressure phase of apatite decomposition and its geochemical significance. Phys Earth Planet Int 44:293–303

Pan Y, Fleet ME (2002) Compositions of the apatite-group minerals: substitution mechanisms and controlling factors. In: Kohn MJ, Rakovan J, Hughes JM (eds) Phosphates. Reviews in mineralogy and geochemistry, vol 48. Mineralogical Society of America, Chantilly, pp 13–49

Popović L, de Waal D, Boeyens JCA (2005) Correlation between Raman wavenumbers and P–O bond lengths in crystalline inorganic phosphates. J Raman Spectrosc 36:2–11

Prowatke S, Klemme S (2006) Trace element partitioning between apatite and silicate melts. Geochim Cosmochim Acta 70:4513–4527

Sha MC, Li Z, Brad RC (1994) Single-crystal elastic constants of fluorapatite, $Ca_5F(PO_4)_3$. J Appl Phys 75:7784–7787

Shannon RD (1976) Revised effective ionic radii and systematic studies of interatomic distances in halides and chalcogenides. Acta Cryst A32:751–767

Snyders R, Music D, Sigumonrong D, Schelnberger B, Jensen J, Schneider JM (2007) Experimental and ab initio study of the mechanical properties of hydroxyapatite. Appl Phys Lett 90:193902

Teraoka K, Ito A, Maekawa K, Onuma K, Tateishi T, Tsutsumi S (1998) Mechanical properties of hydroxyapatite and OH-carbonated hydroxyapatite single crystals. J Dent Res 77:1560–1568

Yoon HS, Newnham RE (1969) Elastic properties of fluorapatite. Am Miner 54:1193–1197